EJNMMI Research

ORIGINAL RESEARCH

Open Access

Dopamine transporter single-photon emission computed tomography-derived radiomics signature for detecting Parkinson's disease

Takuro Shiiba[1*], Kazuki Takano[1], Akihiro Takaki[2] and Shugo Suwazono[3]

Abstract

Background: We hypothesised that the radiomics signature, which includes texture information of dopamine transporter single-photon emission computed tomography (DAT-SPECT) images for Parkinson's disease (PD), may assist semi-quantitative indices. Herein, we constructed a radiomics signature using DAT-SPECT-derived radiomics features that effectively discriminated PD from healthy individuals and evaluated its classification performance.

Results: We analysed 413 cases of both normal control (NC, $n = 101$) and PD ($n = 312$) groups from the Parkinson's Progression Markers Initiative database. Data were divided into the training and two test datasets with different SPECT manufacturers. DAT-SPECT images were spatially normalised to the Montreal Neurologic Institute space. We calculated 930 radiomics features, including intensity- and texture-based features in the caudate, putamen, and pallidum volumes of interest. The striatum uptake ratios (SURs) of the caudate, putamen, and pallidum were also calculated as conventional semi-quantification indices. The least absolute shrinkage and selection operator was used for feature selection and construction of the radiomics signature. The four classification models were constructed using a radiomics signature and/or semi-quantitative indicator. Furthermore, we compared the classification performance of the semi-quantitative indicator alone and the combination with the radiomics signature for the classification models. The receiver operating characteristics (ROC) analysis was used to evaluate the classification performance. The classification performance of $SUR_{putamen}$ was higher than that of other semi-quantitative indicators. The radiomics signature resulted in a slightly increased area under the ROC curve (AUC) compared to $SUR_{putamen}$ in each test dataset. When combined with $SUR_{putamen}$ and radiomics signature, all classification models showed slightly higher AUCs than that of $SUR_{putamen}$ alone.

Conclusion: We constructed a DAT-SPECT image-derived radiomics signature. Performance analysis showed that the current radiomics signature would be helpful for the diagnosis of PD and has the potential to provide robust diagnostic performance.

Keywords: Parkinson's disease, Dopamine transporter, SPECT, Radiomics signature, Texture, Radiomics

Background

Parkinson's disease (PD) is characterised by the degeneration of the nigrostriatal dopamine nerve and the appearance of inclusion bodies containing α-synuclein as the main component (i.e. Lewy bodies) [1–3]. The striatum to which dopamine neurones are projected is a nerve

*Correspondence: takuro.shiiba@fujita-hu.ac.jp

[1] Department of Molecular Imaging, School of Medical Sciences, Fujita Health University, 1-98, Dengakubo, Kutsukake-cho, Toyoake, Aichi 470-1192, Japan
Full list of author information is available at the end of the article

nucleus constituting the basal ganglia and comprises the caudate nucleus and putamen. Dopamine transporter (DAT) single-photon emission computed tomography (SPECT) contributes to the diagnosis of PD and Lewy body dementia by providing a SPECT image reflecting the DAT distribution density in the striatum. Generally, the evaluation of DAT-SPECT images is conducted via visual inspection, frequently supported by semi-quantitative ratios, such as the striatum uptake ratio (SUR) or specific binding ratio (SBR) [4–7]. In visual assessment, information regarding the asymmetry of the left and right striata and the spatial accumulation site of ^{123}I-FP-CIT can be obtained [8–11].

A semi-quantitative analysis is hypothesised to eliminate subjectivity and experience differences among readers. Accurate semi-quantitative values may be helpful in the early diagnosis and prediction of the prognosis of PD [12].

Texture analysis [13] can quantitatively represent the heterogeneity of radiopharmaceutical uptake, such as a tumour, in a region of interest [14, 15]. In recent years, radiomics [16–19], which includes texture analysis, is expected to be used not only for diagnosis but also for predicting patient prognosis and determining treatment effects. Texture analysis has also been applied to DAT-SPECT, and texture features correlate with motor and cognitive functions and contribute to the prediction of motor functions [20]. Rahmin et al. [20] showed that Haralick's texture features [21, 22] in the caudate nucleus correlated with the Unified Parkinson's Disease Rating Scale and disease duration. Among a large number of texture features, only Haralick's texture features by grey-level co-occurrence matrix were used in these studies. In recent years, many software that can easily calculate radiomics features, including morphology, histogram, and texture, have become widely used for study [23]. However, to our knowledge, constructing a radiomics signature from a wide range of candidate features of DAT-SPECT images and evaluating the classification performance of PD have not been reported. Although the conventional semi-quantitative indices have high classification accuracy [24, 25], they do not represent the homogeneity or heterogeneity of radiopharmaceutical distribution in the striatum. The image heterogeneity may become a disturbing factor, which is not well represented through semi-quantitative indices. Therefore, we hypothesised that the radiomics signature, which includes texture information from DAT-SPECT images, may assist semi-quantitative indices. In this study, we constructed a radiomics signature using the radiomics features derived from DAT-SPECT that effectively discriminated PD from healthy individuals and evaluated its classification performance.

Materials and methods

Participants

All data used in this study were obtained from the Parkinson's Progression Markers Initiative (PPMI) database (www.ppmi-info.org/data). At enrolment in PPMI, PD subjects were required to be age 30 years or older, untreated with PD medications (levodopa, dopamine agonists, MAO-B inhibitors, or amantadine), within 2 years of diagnosis, Hoehn and Yahr < 3, and to have either at least two of resting tremor, bradykinesia, or rigidity (must have either resting tremor or bradykinesia) or a single asymmetric resting tremor or asymmetric bradykinesia. All PD subjects underwent dopamine transporter (DAT) imaging with ^{123}I Ioflupane or vesicular monoamine transporter (VMAT-2) imaging with ^{18}F AV133 (Australia only) and were only eligible if DAT or VMAT-2 imaging demonstrated dopaminergic deficit consistent with PD in addition to clinical features of the disease [26]. The dataset contained 790 pre-processed ^{123}I-FP-CIT DAT-SPECT images acquired at the screening stage (accessed on 3 April 2021). This study selected a total of 462 subjects acquired with the two manufacturer's SPECT systems [SIEMENS (dataset 1); 340 and GE (dataset 2); 122]. Dataset 1 excluded subjects whose diagnosis changed during follow-up (NC: 13, PD: 7), resulting in a final total of 320 subjects (NC: 81, PD: 239); dataset 2 included 122 subjects (NC: 20, PD: 102) with no subjects excluded. The remaining data were not used for the following reasons: the number was small when divided by manufacturer, and the manufacturer was unknown. Dataset 1 was divided into the training and test datasets at 7:3 so that the ratio of the NC and PD groups would be constant. Dataset 2 was used as the test dataset 2.

Reconstruction and spatial normalisation of SPECT images

Reconstructed DAT-SPECT images were downloaded from the PPMI website. As per PPMI documentation, pre-processing steps were performed at the Institute for Neurodegenerative Disorders and included the following steps: SPECT imaging and reconstruction: SPECT imaging was acquired at each imaging centre as per the PPMI imaging protocol and sent to the institute for neurodegenerative disorders for processing. SPECT raw projection data were imported to a HERMES (Hermes Medical Solutions, Stockholm, Sweden) system for iterative reconstruction. Iterative reconstruction was performed without filtering. The reconstructed files were transferred to the PMOD (PMOD Technologies, Zurich, Switzerland) for subsequent processing. Attenuation correction ellipses were drawn on the images, and a Chang 0 attenuation correction was applied to images utilising a site-specific μ that was empirically derived from phantom data acquired during

site initiation for the trial. Once attenuation correction was completed, a standard Gaussian three-dimensional (3D) 6.0 mm filter was applied.

Then, the DAT-SPECT images were spatially normalised to Montreal Neurologic Institute (MNI) space using statistical parametric mapping (SPM12, Wellcome Trust Centre for Neuroimaging, London, UK) in MATLAB R2021a (version 9.10, The MathWorks, Inc. Massachusetts, USA). DAT-SPECT images were spatially normalised to the MNI-based template of ^{123}I-FP-CIT [27, 28] using the old normalise function under identical conditions. After spatial normalisation, the radiological technologist with 13-year clinical experience visually assessed for misalignment between DAT-SPECT and the template. Visual assessment of spatial normalisation checked for apparent misalignment in the striatum and whole brain. The pre-processed images were saved in the Neuroimaging Informatics Technology Initiative format using $91 \times 109 \times 91$ isotropic voxels of 2 mm.

Calculation of radiomics features and semi-quantitative indicators

The automated anatomical labelling atlas (AAL) 3 [29] volume of interest (VOI) template was used to calculate the radiomics features. The feature calculation VOIs were the caudate nucleus, putamen, and pallidum (Fig. 1). Radiomics features were calculated using Standardized Environment for Radiomics Analysis (SERA) [30–32] and worked on MATLAB. One hundred and eighty-six image biomarker standardisation initiative-standardised features [23] were calculated using SERA, including 50 first-order features (statistical, histogram, and intensity histogram features) and higher-order136 3D features (Table 1). A total of 558 radiomics features were calculated for the caudate, putamen, and pallidum VOIs. We also calculated the ratio of the caudate to the putamen

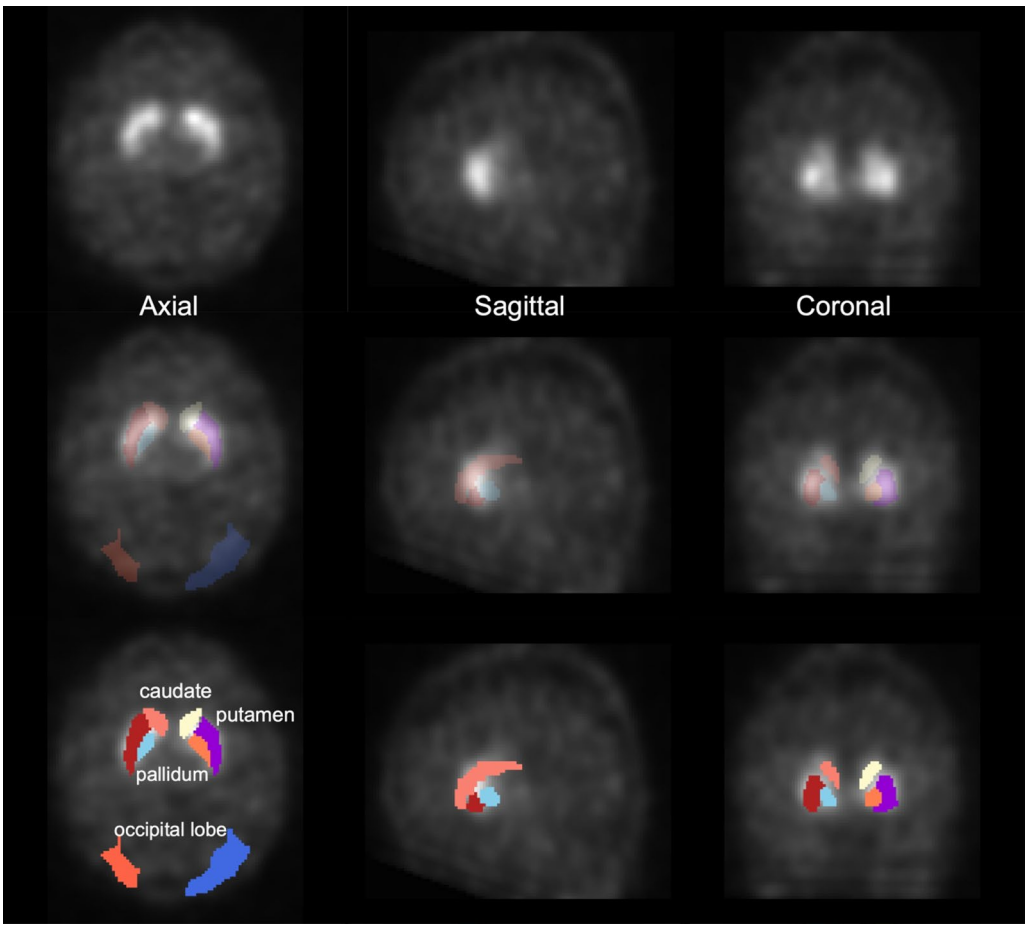

Fig. 1 An example of settings of a voxel of interests for calculating radiomics features and semi-quantitative indices. The upper row indicates after the spatial normalisation dopamine transporter single-photon emission computed tomography, and the middle and lower rows indicate fused image. The coloured area of the middle and lower rows indicates the striatum and background (occipital lobe)

Table 1 Number of radiomics features per region and their family names

Feature family	Number of features
Local intensity	2
Intensity-based statistics	18
Intensity histogram	23
Intensity-volume histogram	7
GLCM	50
GLRLM	32
GLZSM	16
GLDZM	16
NGTDM	5
NGLDM	17
Total	186

GLCM grey-level co-occurrence matrix, *GLRLM* grey-level run-length matrix, *GLZSM* grey-level zone size matrix, *GLDZM* grey-level distance zone matrix, *NGTDM* neighbourhood grey tone difference matrix, *NGLDM* neighbourhood grey-level dependence matrix

or pallidum of radiomics features. All radiomics features were averaged in the bilateral striatum part. These totalled 930 radiomics features. Furthermore, the SUR of the caudate nucleus ($SUR_{caudate}$), putamen ($SUR_{putamen}$), and pallidum ($SUR_{pallidum}$) was calculated as conventional semi-quantification indices. The SUR was calculated using the following formula [33]:

$$\mathrm{SUR}(\%) = \frac{C_{\mathrm{striatum}} - C_{\mathrm{background}}}{C_{\mathrm{background}}} \times 100$$

where $C_{striatum}$ is the average count of the caudate nucleus, putamen, or pallidum, and $C_{background}$ is the average count of the occipital lobe. In addition, the ratios of the caudate to the putamen or pallidum ($CR_{putamen}$, $CR_{pallidum}$) were calculated. All the semi-quantitative indices were averaged in the bilateral striatum and compared between the NC and PD groups, and receiver operating characteristic (ROC) [34] analysis was performed.

Radiomics feature selection and signature construction

The least absolute shrinkage and selection operator (LASSO) [35] function in MATLAB was used to select effective features from the radiomics features. Multicollinearity of features was not considered in this study because LASSO can feature selection with suppressed multi-collinearity [36]. All radiomics features were z-scored to mean 0 and standard deviation 1.0 before being inputted to LASSO. LASSO permits the estimation and selection of explanatory variables [37, 38], that is, radiomics features with nonzero coefficients. For the selection of radiomics features using LASSO, a tenfold cross-validation test was conducted using the training set. Furthermore, the linear combination sum of five radiomics features with nonzero coefficients was used as the radiomics signature. We compared the classification performance of the radiomics signature and semi-quantitative indicator that showed the highest classification performance.

Classification model construction with radiomics signature and semi-quantitative indicator

The classification models for the NC and PD groups were constructed using the radiomics signature and/or semi-quantitative indicator. The four classifiers used were support vector machine (SVM), k-nearest neighbour (KNN), linear discriminant analysis (LDA), and decision tree. The main parameters of each classifier were as follows: SVM (BoxConstraint = 1, KernelScale = 1, KernelFunction = polynomial [order = 3]), KNN (NumNeighbours = 1, Distance = Minkowski, Exponent = 2), LDA (Gamma = 0), and decision tree (MinLeafSize = 1, MinParentSize = 10). The features used were radiomics signature alone, semi-quantitative indicator alone, and both. The training set was used to train the classifier, and the performance of each classification model was evaluated using each test dataset. Classification performance was evaluated using the area under the ROC curve (AUC).

Statistical analyses

The radiomics signature and SURs in the NC and PD groups were tested for significant differences using the Wilcoxon rank-sum test. ROC analysis was performed using semi-quantitative indicators and radiomics signature. We used the DeLong [39] test to examine the differences in AUCs, and for multiple comparisons, the Bonferroni correction was performed. The sensitivity, specificity, and accuracy of semi-quantitative indices and radiomics signature were calculated using the optimal cut-off values determined based on ROC analysis. The optimal cut-off values for radiomics signature and semi-quantitative indices were calculated using the training dataset. At the same time, sensitivity, specificity, and accuracy were assessed using test datasets 1 and 2.

Differences were considered statistically significant at $P < 0.05$. All statistical analyses were performed using RStudio (version 1.4.1106).

Results

Table 2 shows the characteristics of the subjects in this study. In dataset 1, no cases were excluded due to failure of spatial normalisation, whereas in dataset 2, 28 subjects of PD were excluded due to failure of spatial normalisation, resulting in 93 subjects (NC: 20, PD 73).

Table 2 Characteristics of subjects

Characteristics	Dataset 1 (SIEMENS)		Dataset 2 (GE)	
	NC	PD	NC	PD
Number of subjects	81	239	20	73
Male/female	57/24	151/88	13/7	53/20
Age	61.2 ± 9.5	59.8 ± 11	60.3 ± 13	60.8 ± 10
Age of diagnosis	NA	60.7 ± 9.5	NA	59.0 ± 11
Hoehn and Yahr stage	0.01 ± 0.1	1.58 ± 0.5	0.00 ± 0.0	1.64 ± 0.5
MDS-UPDRS III	1.0 ± 1.9	21.8 ± 9.3	0.89 ± 2.2	17.0 ± 9.9
MoCA	28.2 ± 1.1	27.3 ± 2.3	28.6 ± 1.2	27.1 ± 3.3

MDS-UPDRS movement disorder society-unified Parkinson's disease rating scale, *MoCA* Montreal Cognitive Assessment, *NC* normal control, *PD* Parkinson's disease, *NA* not applicable

The number of subjects included 320 subjects for dataset 1 and 93 subjects for dataset 2.

Figures 2 and 3 show the distribution of semi-quantitative indices for test datasets 1 and 2. There was a significant difference between the NC and PD groups in all of the SURs ($P < 0.001$). Caudate-to-putamen or pallidum ratios showed significant differences ($P < 0.001$) between NC and PD, except for $CR_{pallidum}$ ($P = 0.064$) in test dataset 1.

Figure 4 shows the ROC curves of the semi-quantitative indices for each test dataset. The AUCs and 95% confidence interval (CI) of SURs and CRs for test dataset 1 were, in order from highest to lowest, as follows: $SUR_{putamen}$ (0.980, 0.951–1.000), $SUR_{pallidum}$ (0.907, 0.831–0.982), $CR_{putamen}$ (0.885, 0.805–0.965), $SUR_{caudate}$ (0.877, 0.793–0.960), and $CR_{pallidum}$ (0.625, 0.502–0.747). Similarly, for test dataset 2 as follows: $SUR_{putamen}$ (0.929, 0.879–0.979), $SUR_{pallidum}$ (0.925, 0.872–0.977), $CR_{putamen}$ (0.848, 0.749–0.834), $SUR_{caudate}$ (0.834, 0.740–0.927), and $CR_{pallidum}$ (0.780, 0.687–0.873). There was a significant difference between $SUR_{putamen}$ and other SURs or CRs ($P < 0.05$) for test dataset 1. For test dataset 2, there was a significant difference between $SUR_{putamen}$ and two indices ($SUR_{caudate}$ and $CR_{pallidum}$) ($P < 0.05$).

Table 3 shows the radiomics features and coefficients selected by LASSO in the training set. The lambda value was set to 0.0967, and five radiomics features were selected. The selected radiomics features included four putamen features and $CR_{pallidum}$. Coefficients and radiomics features were used to construct the radiomics signature:

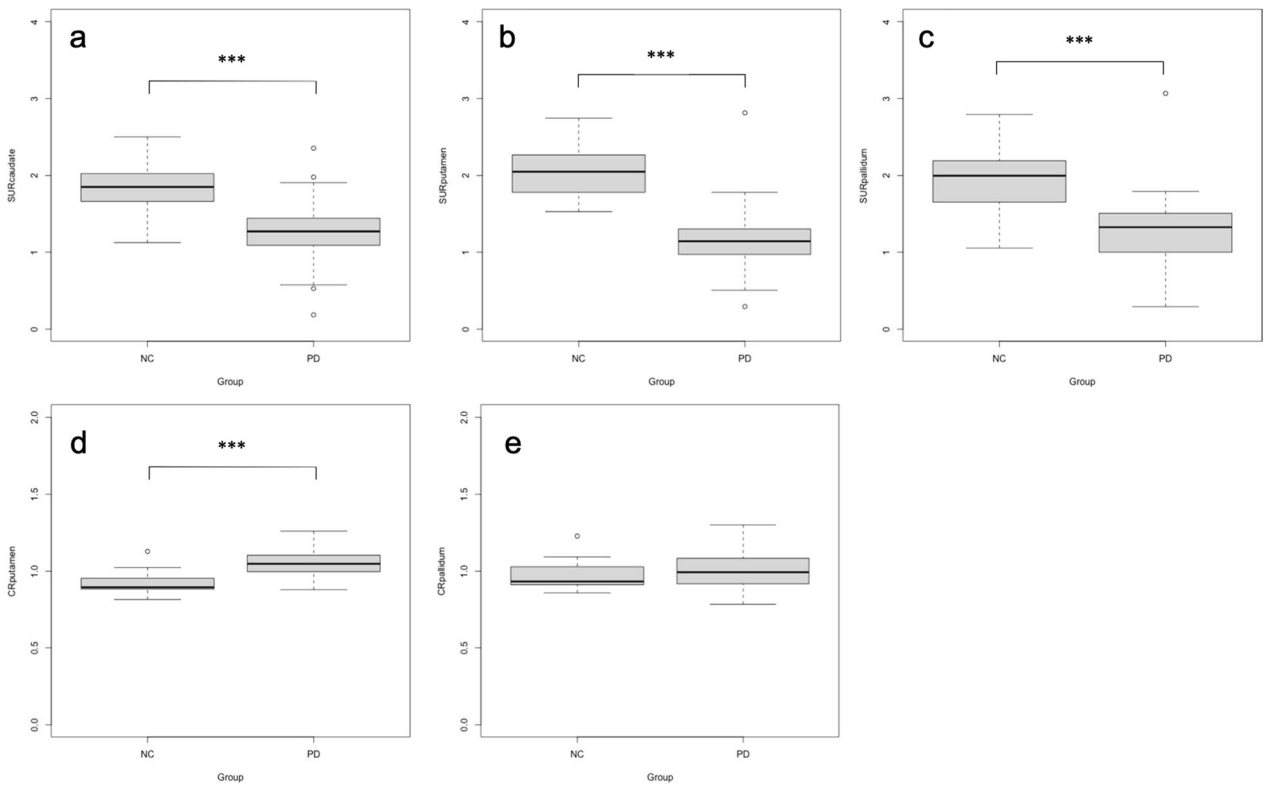

Fig. 2 Striatum uptake ratio (SUR) and caudate ratio (CR) between the normal control and Parkinson's disease for test dataset 1. Box-and-whisker plots indicate the semi-quantitative indices distribution. **a** $SUR_{caudate}$, **b** $SUR_{putamen}$, **c** $SUR_{pallidum}$; **d,** $CR_{putamen}$, **e** $CR_{pallidum}$. $^{***}P < 0.001$

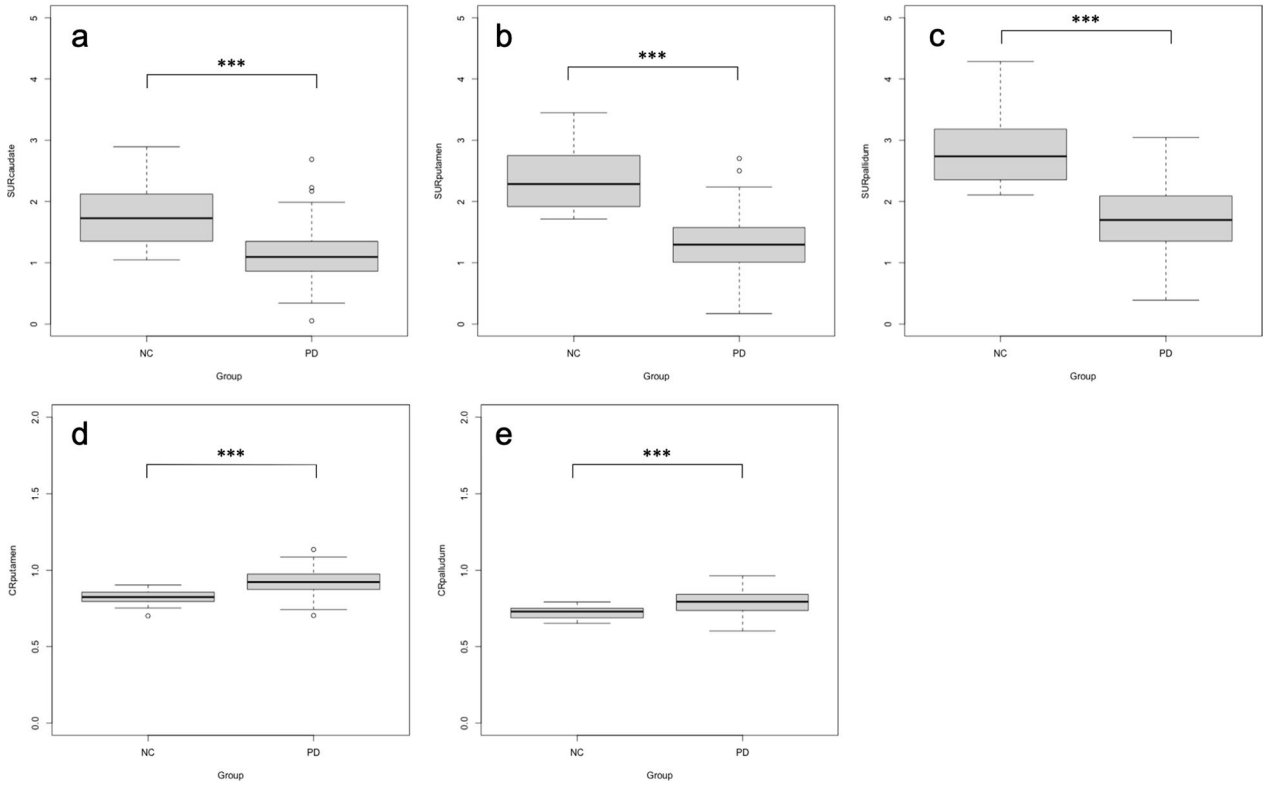

Fig. 3 Striatum uptake ratio (SUR) and caudate ratio (CR) between the normal control and Parkinson's disease for test dataset 2. Box-and-whisker plots indicate the semi-quantitative indices distribution. **a** $SUR_{caudate}$, **b** $SUR_{putamen}$, **c** $SUR_{pallidum}$; **d,** $CR_{putamen}$, **e** $CR_{pallidum}$. $^{***}P < 0.001$

Radiomics signature $= -0.00863 \times \text{ih\_median}_{putamen} - 0.18100 \times \text{dzm\_zdnu\_3D}_{putamen} - 0.02485 \times \text{ngl\_dcnu\_3D}_{putamen} - 0.00001 \times \text{ngl\_dcnu\_norm\_3D}_{putamen} - 0.05259 \times \text{szm\_lzlge\_3D}_{CRpallidum}$.

Figure 5 shows the distribution of radiomics signatures between the NC and PD groups. There was a significant difference between the NC and PD groups ($P < 0.001$) for test datasets 1 and 2.

A comparison of the ROC curves for the radiomics signature and $SUR_{putamen}$ is shown in Fig. 6. In the test dataset 1, the AUCs of the radiomics signature and $SUR_{putamen}$ were 0.990 (95% CI, 0.976–1.00) and 0.980 (95% CI, 0.951–1.00), respectively ($P = 0.302$). In the test dataset 2, the AUCs of the radiomics signature and $SUR_{putamen}$ were 0.986 (95% CI, 0.967–1.00) and 0.929 (95% CI, 0.879–0.979), respectively ($P = 0.041$).

Table 4 shows the classification accuracy of the radiomics signature and $SUR_{putamen}$. The accuracy, sensitivity, and specificity of the radiomics signature and $SUR_{putamen}$ were 95.8%, 98.6%, and 88.0% and 95.8%, 97.2%, and 92.0% and 96.8%, 100%, and 85.0% and 82.8%, 78.1%, and 100% for the test datasets 1 and 2, respectively.

Tables 5 and 6 show the AUCs of each classification model when radiomics signature alone, $SUR_{putamen}$ alone, and both features were combined. There were no significant differences in the AUCs between $SUR_{putamen}$ alone and in combination with $SUR_{putamen}$ and radiomics signature for test dataset 1. However, the AUC was better in all models when combined with $SUR_{putamen}$ and radiomics signature compared to $SUR_{putamen}$ alone.

A similar trend to test dataset 1 was observed in test dataset 2. Radiomics signature in combination with SUR-putamen improved AUC for KNN and LDA models.

Discussion

In this study, we constructed and evaluated the potential of a radiomics signature derived from DAT-SPECT images to classify the NC and PD groups.

The main findings of this study are as follows. First, radiomics signature may have a similar or slightly higher classification performance than semi-quantitative indicators. Second, the combination of radiomics signature and semi-quantitative indicator as features for the classification models would improve the classification performance compared to that of the semi-quantitative indicator alone.

$SUR_{putamen}$ showed the highest classification performance among the semi-quantitative indices for each

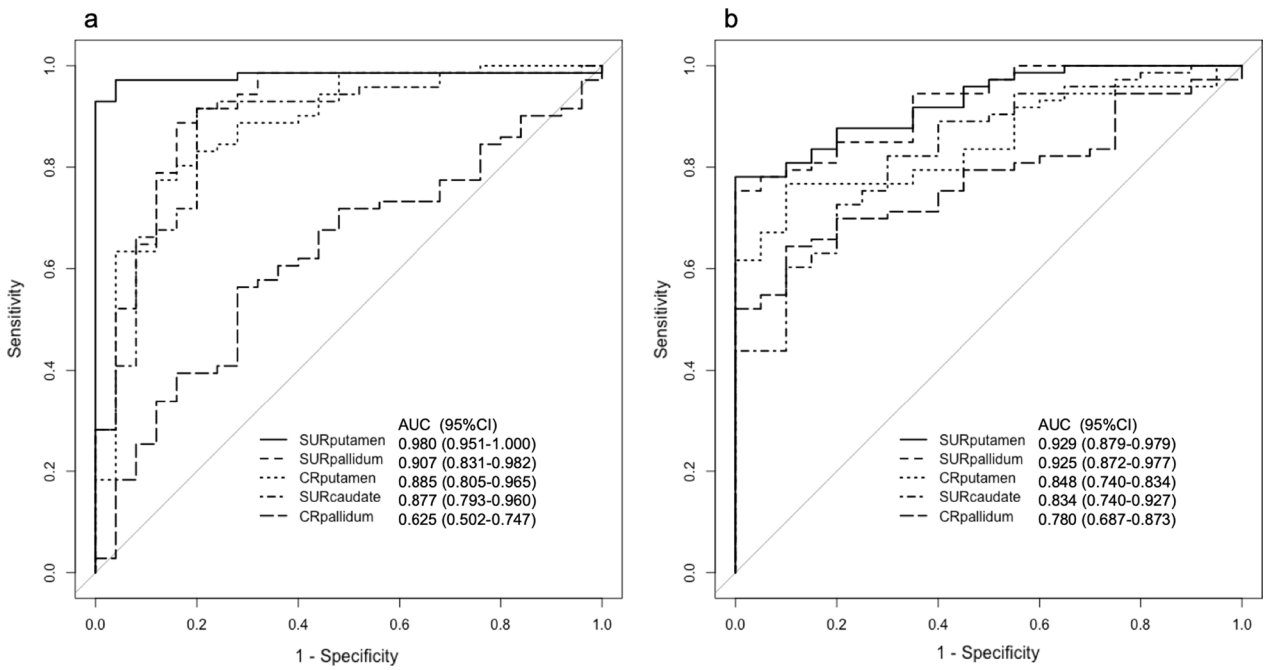

Fig. 4 Receiver operating curves for semi-quantitative indices. **a** The AUCs and 95% confidence interval (CI) for the test dataset 1of semi-quantitative indices in each region were $SUR_{putamen}$ (0.980, 0.951–1.000), $SUR_{pallidum}$ (0.907, 0.831–0.982), $CR_{putamen}$ (0.885, 0.805–0.965), $SUR_{caudate}$ (0.877, 0.793–0.960), and $CR_{pallidum}$ (0.625, 0.502–0.747). There was a significant difference between $SUR_{putamen}$ and other semi-quantitative indices ($P < 0.001$). **b** The AUCs and 95% confidence interval (CI) for the test dataset 2 of semi-quantitative indices in each region were $SUR_{putamen}$ (0.929, 0.879–0.979), $SUR_{pallidum}$ (0.925, 0.872–0.977), $CR_{putamen}$ (0.848, 0.740–0.834), $SUR_{caudate}$ (0.834, 0.740–0.927), and $CR_{pallidum}$ (0.780, 0.687–0.873). There was a significant difference between $SUR_{putamen}$ and $SUR_{caudate}$, ($P < 0.01$), or $CR_{pallidum}$ ($P < 0.05$). *AUC* area under the curve, *CI* confidence interval, *SUR* striatum uptake ratio, *CR* caudate ratio

Table 3 Radiomics features and coefficients selected using LASSO

Feature family	Feature name (tag name)	Region	Coefficients
Intensity histogram	Median (ih_median)	Putamen	−0.00863
GLDZM (3D)	Zone distance non-uniformity (dzm_zdnu_3D)	Putamen	−0.18100
NGLDM (3D)	Dependence count non-uniformity normalised (ngl_dcnu_norm_3D)	Putamen	−0.02485
NGLDM (3D)	Dependence count non-uniformity normalised (ngl_dcnu_norm_3D)	Putamen	−0.00001
GLSZM (3D)	Large zone low grey-level emphasis (szm_lzlge_3D)	Caudate/pallidum	−0.05259

GLDZM grey-level distance zone matrix, *NGLDM* neighbourhood grey-level dependence matrix, GL*SZM* grey-level size zone matrix

region obtained from spatially normalised DAT-SPECT images. It is well known that ^{123}I-FP-CIT decline began in the caudal putamen loss in patients with PD [40]. Therefore, $SUR_{putamen}$ reflected the difference in radiopharmaceutical accumulation in the putamen between the NC and PD groups and showed high classification performance. The high classification performance of the semi-quantitative indicator of the putamen is consistent with those of several previous studies [41–43].

For radiomics feature selection, the most common region to which the eight features selected by LASSO belonged to the putamen, followed by the pallidum. This is because radiopharmaceuticals accumulate less from the putamen in PD, similar to the above. Radiomics features reflect the heterogeneity of radiopharmaceutical accumulations in VOIs. GLDZM (zone distance non-uniformity; tag name, $dzm\_zdnu\_3D_{putamen}$), which had the most significant coefficient, is a matrix that shows how far the connected regions with the same concentration value are from the edge of the region of interest. The dzm_zdnu_3D measures the distribution of zone counts over the different zone distances and is low when the zone counts are equally distributed along with the zone distances. In the putamen region, $dzm\_zdnu\_3D_{putamen}$

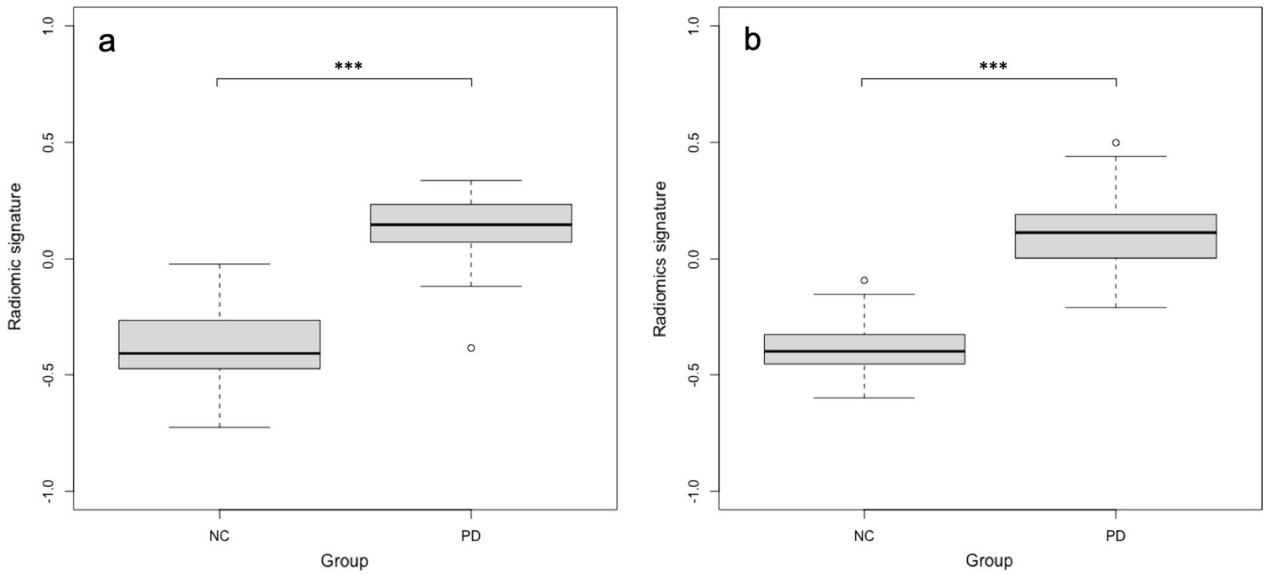

Fig. 5 Comparison of radiomics signature between the normal control and Parkinson's disease. Box-and-whisker plots indicate the radiomics signature distribution. **a** Test dataset 1, **b** test dataset 2. $^{***}P < 0.001$

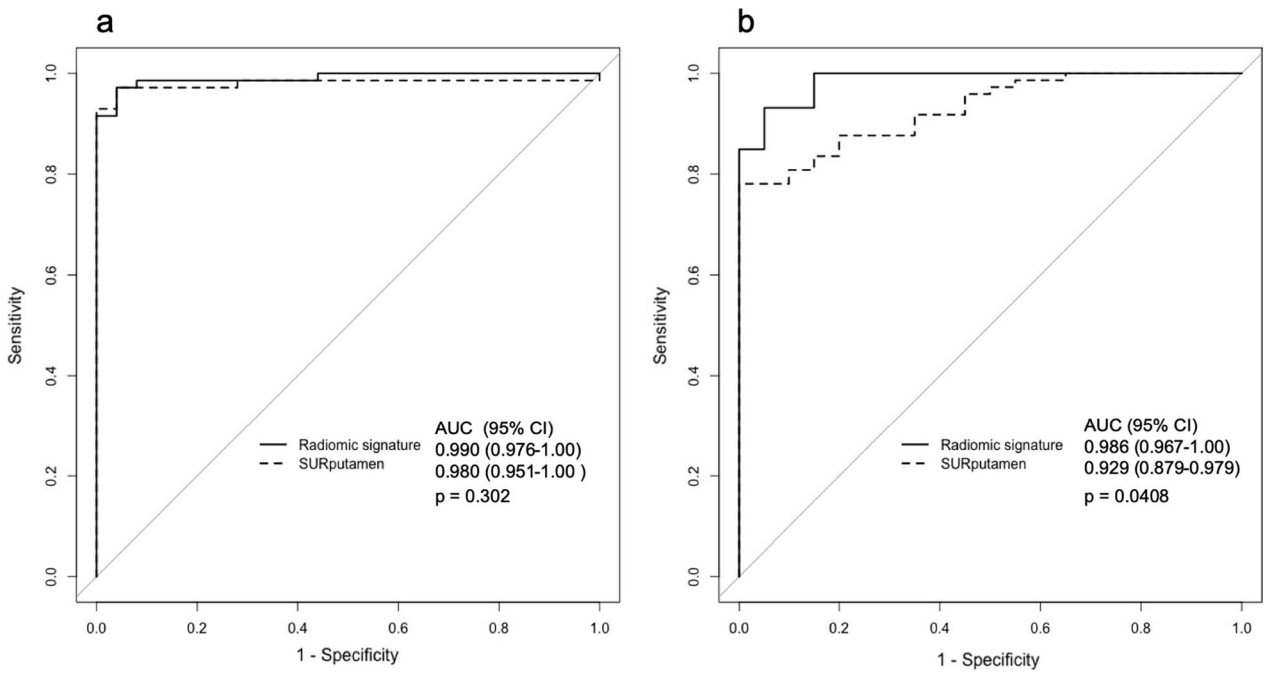

Fig. 6 Comparison of receiver operating curves between radiomics signature and striatum uptake ratio of the putamen. **a** The AUCs for the test dataset 1of the radiomics signature and $SUR_{putamen}$ were 0.990 (95% CI, 0.976–1.00) and 0.980 (95% CI, 0.951–1.00), respectively ($P = 0.302$). **b** The AUCs for the test dataset 2 of the radiomics signature and $SUR_{putamen}$ were 0.986 (95% CI, 0.967–1.00) and 0.929 (95% CI, 0.879–0.979), respectively ($P = 0.041$). *AUC* area under the curve, *CI* confidence interval, *SUR* striatum uptake ratio

in the PD group was significantly lower than in the PD group (data not shown). This result indicates that the number of connected zones of PD was lower than that of the NC group. Comparing the histogram features in the putamen region of NC and PD in dataset 1, uniformity (0.03 vs 0.04, $p < 0.001$), kurtosis (−0.83 vs 0.24, $p < 0.001$),

Table 4 Classification accuracy of radiomics signature and $SUR_{putamen}$ for the test datasets

	Test dataset 1		Test dataset 2	
	Radiomics signature	$SUR_{putamen}$	Radiomics signature	$SUR_{putamen}$
Accuracy (%)	95.8	95.8	96.8	82.8
Sensitivity (%)	98.6	97.2	100	78.1
Specificity (%)	88.0	92.0	85.0	100

SUR striatum uptake ratio

and skewness (0.21 vs 0.82, $p < 0.001$) of PD were higher than those of NC. These results indicate that voxel values in the putamen region of NC were widely distributed, whereas they tend to be biased towards lower voxel values in PD. In other words, the number of connected voxels per connected region was higher in PD because the voxel values were similar to each neighbouring voxel [the number of connected regions (= zone counts) was lower]. On the other hand, NCs are more likely to have different neighbouring voxel values, which means they may have fewer connected voxels per connected region and a larger number of connected regions than PD. In PD, the loss of dopamine transporters progresses from the posterior to the anterior of the putamen. The lower dzm_dcnu_3D in putamen for PD suggests large areas of reduced dopamine transporter. Based on the results of the two test datasets for radiomics signature, texture information of the putamen can be a robust and powerful indicator for the differentiation of PD.

The radiomics signature showed a similar or slightly higher classification performance between the PD and NC groups than that of $SUR_{putamen}$. Furthermore, when the various classification models were constructed using both the radiomics signature and $SUR_{putamen}$ as features, the classification performance was better than that of $SUR_{putamen}$ alone. This result suggests that the radiomics signature provides robust texture information to supplement the semi-quantitative indicators. Iwabuchi et al. [44] reported that the combined diagnostic accuracy of the three types of indices, SBR, putamen-to-caudate ratio (PCR), and fractal dimension (or asymmetry index), used for SVM improves diagnostic accuracy. Generally, semi-quantitative indicators assess the quantity of radiopharmaceuticals, and their spatial distribution depends on visual assessment. Adding an indicator for the radiopharmaceutical spatial distribution (e.g. texture information, PCR, fractal dimension) to the semi-quantitative indicator would improve the diagnostic accuracy. We believe that the combination of the semi-quantitative indicator and radiomics signature would lead to the development of highly accurate automatic diagnosis or diagnostic assistant models. On the other hand, constructing a radiomics signature is more complicated and time-consuming than conventional semi-quantitative indicators such as SBR. The meaning indicated by the radiomics signature might be difficult to understand for physicians.

This study investigated the robustness of the radiomics signature by using two test datasets. The radiomics signature showed a high classification performance in

Table 5 Classification performance of various classification models using radiomics signature and $SUR_{putamen}$ for test dataset 1

Classifier	Features AUC (95% CI)			*P* value ($SUR_{putamen}$ vs. combination)
	Radiomics signature	$SUR_{putamen}$	Combination	
SVM	0.983 (0.943–0.996)	0.983 (0.944–0.996)	0.991 (0.967–0.999)	0.333
KNN	0.930 (0.835–0.979)	0.918 (0.817–0.972)	0.950 (0.866–0.991)	0.261
LDA	0.990 (0.956–0.999)	0.980 (0.910–0.997)	0.987 (0.931–1.000)	0.167
Decision tree	0.970 (0.877–0.999)	0.965 (0.909–0.988)	0.970 (0.879–0.998)	0.825

SVM support vector machine, *KNN* k-nearest neighbour, *LDA* linear discriminant analysis, *SUR* striatum uptake ratio, *AUC* area under the curve, *CI* confidence interval

Table 6 Classification performance of various classification models using radiomics signature and $SUR_{putamen}$ for test dataset 2

Classifier	Features AUC (95% CI)			*P* value ($SUR_{putamen}$ vs. combination)
	Radiomics signature	$SUR_{putamen}$	Combination	
SVM	0.977 (0.934–0.994)	0.921 (0.847–0.963)	0.940 (0.746–0.995)	0.755
KNN	0.896 (0.768–0.998)	0.857 (0.729–0.941)	0.997 (0.986–1.000)	0.006
LDA	0.986 (0.947–0.998)	0.929 (0.858–0.967)	0.996 (0.961–1.000)	0.009
Decision tree	0.973 (0.929–0.990)	0.928 (0.858–0.966)	0.952 (0.909–0.985)	0.300

SVM support vector machine, *KNN* k-nearest neighbour, *LDA* linear discriminant analysis, *SUR* striatum uptake ratio, *AUC* area under the curve, *CI* confidence interval

each test dataset, which could be a robust indicator for PD and NC classification; $SUR_{putamen}$ also showed a high classification performance, which was slightly lower in test dataset 2. The differences in image quality due to SPECT system were reflected in the SURs [45]. Furthermore, the difference in image quality may also affect the accuracy of spatial normalisation. In dataset 2, 28 cases of spatial normalisation failed. This failure was due to the lower prefrontal cortex and cerebellar areas omitting from the field of view. These SPECT images were taken at the same facility and may be an issue of imaging technique. In this study, VOI settings based on the AAL label images were applied to DAT-SPECT images after spatial normalisation. Buchert et al. [46] reported that the diagnostic performance of the caudate SBR was lower than that of putamen when using the VOI of AAL. Nonokuma et al. [47] used an MRI-based ROI similar to the AAL VOI but failed to accurate radioactivity in the caudate nucleus. They described that the tissue mixture effect due to the dilated anterior horn of the lateral ventricle might decrease the radioactivity in the caudate nucleus and shift the peak caudally. Similarly, our results also showed that the $SUR_{caudate}$ and its classification performance tend to be lower than the putamen. Therefore, using an optimal VOI to calculate the SUR is necessary. Several researchers [48, 49] reported that PD patients had significantly lower DAT uptake ratios in the pallidum than healthy controls. Based on these reports, we also settled pallidum VOI, and $SUR_{pallidum}$ of PD indicated lower than that of NC. However, it is not easy to accurately spatial normalise and delimit each region on DAT-SPECT. Therefore, we should be careful in interpreting each VOI result.

This study had some limitations. First, we employed a single-manufacturing SPECT system to exclude the influence of the differences in SPECT image quality among manufacturers. Consequently, there was an imbalance between the NC and PD groups. Therefore, it is necessary to investigate an increase in the number of patients. Second, wavelet features were not included in the radiomics features. Because SERA does not support wavelet analysis, other software should be used. Finally, we did not consider differences in the striatum laterally based on a previous report that showed lower accuracy for the asymmetry index than that of SBR and PCR [24]. As lateral differences might be useful for distinguishing between PD in the early stage and other Parkinsonism, such as progressive supranuclear palsy of the Parkinsonism subtype [50], signature construction is required.

Conclusions

In conclusion, the radiomics signature derived from DAT-SPECT images could help distinguish between NC and PD. Furthermore, the classification performance of various classification models was improved using both radiomics signature and semi-quantitative indicators. Therefore, a radiomics signature, which includes texture information, could provide a robust diagnostic performance when used with semi-quantitative indicators.

Abbreviations

DAT-SPECT: Dopamine transporter single-photon emission computed tomography; PD: Parkinson's disease; NC: Normal control; SUR: Striatum uptake ratio; ROC: Receiver operating characteristics; AUC: Area under the ROC curve; SBR: Specific binding ratio; 3D: Three-dimensional; MNI: Montreal Neurologic Institute; AAL: Automated anatomical labelling atlas; VOI: Voxel of interest; SERA: Standardized Environment for Radiomics Analysis; $SUR_{caudate}$: SUR of the caudate nucleus; $SUR_{putamen}$: SUR of the putamen; $SUR_{pallidum}$: SUR of the pallidum; $CR_{putamen}$: Ratio of the caudate to the putamen; $CR_{pallidum}$: Ratio of the caudate to the pallidum; LASSO: Least absolute shrinkage and selection operator; MSE: Mean square error; SVM: Support vector machine; KNN: K-nearest neighbour; LDA: Linear discriminant analysis; CI: Confidence interval; PCR: Putamen-to-caudate ratio.

Acknowledgements

Data used in the preparation of this article were obtained from the PPMI database. PPMI—a public–private partnership—is funded by the Michael J. Fox Foundation for Parkinson's Research funding partners 4D Pharma, Abbvie, Acurex Therapeutics, Allergan, Amathus Therapeutics, ASAP, Avid Radiopharmaceuticals, Bial Biotech, Biogen, BioLegend, Bristol-Myers Squibb, Calico, Celgene, Dacapo Brain Science, Denali, The Edmond J. Safra Foundation, GE Healthcare, Genentech, GlaxoSmithKline, Golub Capital, Handl Therapeutics, Insitro, Janssen Neuroscience, Lilly, Lundbeck, Merck, Meso Scale Discovery, Neurocrine Biosciences, Pfizer, Piramal, Prevail, Roche, Sanofi Genzyme, Servier, Takeda, Teva, UCB, Verily, and Voyager Therapeutics.

Author contributions

All authors contributed to the conception and design of the study. Material preparation, data collection, and analysis were performed by TS and KT. Spatially normalised SPECT was visually assessed by TS. TS wrote the original draft of the manuscript, and KT, AT, and SS wrote the review and edited the previous versions of the manuscript. All authors have read and approved the final manuscript.

Funding

This work was supported by the JSPS KAKENHI (Grant Number: 18K15565 and 21K15791).

Availability of data and materials

The datasets analysed during the current study are available in the PPMI repository, https://www.ppmi-info.org.

Declarations

Ethics approval and consent to participate

All the clinical and imaging data acquired in this study were conducted in accordance with the Declaration of Helsinki after the approval of the local ethics committees of the sites participating in the PPMI. The relevant local institutional review boards approved the PPMI protocol, and written informed consent was obtained from all patients prior to inclusion. Additional approval was obtained from the Ethics Committee of Fujita Health University (HM21–074) for data analysis.

Consent for publication

Not applicable.

Competing interests

The authors declare that they have no competing interests.

Author details
[1]Department of Molecular Imaging, School of Medical Sciences, Fujita Health University, 1-98, Dengakubo, Kutsukake-cho, Toyoake, Aichi 470-1192, Japan. [2]Department of Radiological Technology, Faculty of Fukuoka Medical Technology, Teikyo University, 6-22 Misakimachi, Omuta-shi, Fukuoka 836-8505, Japan. [3]Department of Neurology and Center for Clinical Neuroscience, National Hospital Organization Okinawa National Hospital, 3-20-14 Ganeko, Ginowan 901-2214, Okinawa, Japan.

Received: 3 February 2022 Accepted: 21 June 2022
Published online: 27 June 2022

References

1. Tolosa E, Wenning G, Poewe W. The diagnosis of Parkinson's disease. Lancet Neurol. 2006;5:75–86.
2. Booth TC, Nathan M, Waldman AD, Quigley AM, Schapira AH, Buscombe J. The role of functional dopamine-transporter SPECT imaging in parkinsonian syndromes, part 1. Am J Neuroradiol. 2015;36(2):229–35.
3. Booth TC, Nathan M, Waldman AD, Quigley AM, Schapira AH, Buscombe J. The role of functional dopamine-transporter SPECT imaging in Parkinsonian syndromes, part 2. Am J Neuroradiol. 2015;36:236–44.
4. Darcourt J, Booij J, Tatsch K, Varrone A, Vander Borght T, Kapucu ÖL, et al. EANM procedure guidelines for brain neurotransmission SPECT using123I-labelled dopamine transporter ligands, version 2. Eur J Nucl Med Mol Imaging. 2010;37:443–50.
5. Tossici-Bolt L, Hoffmann SMA, Kemp PM, Mehta RL, Fleming JS. Quantification of [123I]FP-CIT SPECT brain images: an accurate technique for measurement of the specific binding ratio. Eur J Nucl Med Mol Imaging. 2006;33:1491–9.
6. Benamer HTS, Patterson J, Wyper DJ, Hadley DM, Macphee GJA, Grosset DG. Correlation of Parkinson's disease severity and duration With I-FP-CIT SPECT striatal uptake. Mov Disord. 2000;15:692–8.
7. Bonab AA, Fischman AJ, Alpert NM. Comparison of 4 methods for quantification of dopamine transporters by SPECT with [123I]IACFT. J Nucl Med. 2000;41:1086–92.
8. Kahraman D, Eggers C, Schicha H, Timmermann L, Schmidt M. Visual assessment of dopaminergic degeneration pattern in 123I-FP-CIT SPECT differentiates patients with atypical parkinsonian syndromes and idiopathic Parkinson's disease. J Neurol. 2012;259:251–60.
9. Habraken JB, Booij J, Slomka P, Sokole EB, van Royen EA. Quantification and visualization of defects of the functional dopaminergic system using an automatic algorithm. J Nucl Med. 1999;40:1091–7.
10. Eggers C, Kahraman D, Fink GR, Schmidt M, Timmermann L. Akinetic-rigid and tremor-dominant Parkinson's disease patients show different patterns of FP-CIT Single photon emission computed tomography. Mov Disord. 2011;26:416–23.
11. Lloyd JJ, Petrides G, Donaghy PC, Colloby SJ, Attems J, O'Brien JT, et al. A new visual rating scale for Ioflupane imaging in Lewy body disease. NeuroImage: Clin. 2018;20:823–9.
12. Bajaj N, Hauser RA, Grachev ID. Clinical utility of dopamine transporter single photon emission CT (DaT-SPECT) with (123I) ioflupane in diagnosis of parkinsonian syndromes. J Neurol Neurosurg Psychiatr. 2013;84(11):1288–95.
13. Ojala T, Pietikäinen M, Harwood D. A comparative study of texture measures with classification based on featured distributions. Pattern Recognit Pergamon. 1996;29:51–9.
14. Orlhac F, Soussan M, Maisonobe JA, Garcia CA, Vanderlinden B, Buvat I. Tumor texture analysis in 18F-FDG PET: relationships between texture parameters, histogram indices, standardized uptake values, metabolic volumes, and total lesion glycolysis. J Nucl Med. 2014;55:414–22.
15. Chen S, Harmon S, Perk T, Li X, Chen M, Li Y, et al. Diagnostic classification of solitary pulmonary nodules using dual time 18F-FDG PET/CT image texture features in granuloma-endemic regions. Sci Rep. 2017;7(1):1–8.
16. van Timmeren JE, Cester D, Tanadini-Lang S, Alkadhi H, Baessler B. Radiomics in medical imaging—"how-to" guide and critical reflection. Insights Imaging. 2020;11:91.
17. Schernberg A, Orlhac F, Sun R, Chargari C, Dercle L, Deutsch E, et al. Radiomics in nuclear medicine applied to radiation therapy: methods, pitfalls, and challenges. Int J Radiat Oncol Biol Phys. 2018;102:1117–42.
18. Hirata K, Shiga T. Radiomics in nuclear medicine. Nihon Hoshasen Gijutsu Gakkai Zasshi. 2018;74:1368–76.
19. Lambin P, Rios-Velazquez E, Leijenaar R, Carvalho S, van Stiphout RGPM, Granton P, et al. Radiomics: extracting more information from medical images using advanced feature analysis. Eur J Cancer Pergamon. 2012;48:441–6.
20. Rahmim A, Huang P, Shenkov N, Fotouhi S, Davoodi-Bojd E, Lu L, et al. Improved prediction of outcome in Parkinson's disease using radiomics analysis of longitudinal DAT SPECT images. NeuroImage: Clin. 2017;16:539–44.
21. Haralick RM, Dinstein I, Shanmugam K. Textural features for image classification. IEEE Trans Syst Man Cybern. 1973;3(6):610–21.
22. Haralick RM. Statistical and structural approaches to texture. Proc IEEE. 1979;67:786–804.
23. Zwanenburg A, Vallières M, Abdalah MA, Aerts HJWL, Andrearczyk V, Apte A, et al. The image biomarker standardization initiative: standardized quantitative radiomics for high-throughput image-based phenotyping. Radiology. 2020;295:328–38. https://doi.org/10.1148/radiol.2020191145.
24. Iwabuchi Y, Nakahara T, Kameyama M, Yamada Y, Hashimoto M, Matsusaka Y, et al. Impact of a combination of quantitative indices representing uptake intensity, shape, and asymmetry in DAT SPECT using machine learning: comparison of different volume of interest settings. EJNMMI Res. 2019. https://doi.org/10.1186/s13550-019-0477-x.
25. Wenzel M, Milletari F, Krüger J, Lange C, Schenk M, Apostolova I, et al. Automatic classification of dopamine transporter SPECT: deep convolutional neural networks can be trained to be robust with respect to variable image characteristics. Eur J Nucl Med Mol Imaging. 2019;46:2800–11.
26. Marek K, Chowdhury S, Siderowf A, Lasch S, Coffey CS, Caspell-Garcia C, et al. The Parkinson's progression markers initiative (PPMI)—establishing a PD biomarker cohort. Ann Clin Transl Neurol. 2018;5:1460–77.
27. Salas-Gonzalez D, Górriz JM, Ramírez J, Illán IA, Lang EW. Linear intensity normalization of FP-CIT SPECT brain images using the α-stable distribution. Neuroimage. 2013;65:449–55.
28. Salas-Gonzalez D, Górriz JM, Ramírez J, Illán IA, Padilla P, Martínez-Murcia FJ, et al. Building a FP-CIT SPECT brain template using a posterization approach. Neuroinformatics. 2015;13:391–402.
29. Rolls ET, Huang CC, Lin CP, Feng J, Joliot M. Automated anatomical labelling atlas 3. Neuroimage. 2020;206:116189.
30. Feliciani G, Mellini L, Carnevale A, Sarnelli A, Menghi E, Piccinini F, et al. The potential role of MR based radiomic biomarkers in the characterization of focal testicular lesions. Sci Rep. 2021;11(1):1–9.
31. Du D, Feng H, Lv W, Ashrafinia S, Yuan Q, Wang Q, et al. Machine learning methods for optimal radiomics-based differentiation between recurrence and inflammation: application to nasopharyngeal carcinoma post-therapy PET/CT images. Mol Imaging Biol. 2020;22(3):730–8.
32. S. Ashrafinia Quantitative nuclear medicine imaging using advanced image reconstruction and radiomics. (2019)
33. Crespo C, Gallego J, Cot A, Falcón C, Bullich S, Pareto D, et al. Quantification of dopaminergic neurotransmission SPECT studies with 123I-labelled radioligands. A comparison between different imaging systems and data acquisition protocols using Monte Carlo simulation. Eur J Nucl Med Mol Imaging. 2008;35(7):1334–42.
34. Hanley JA, McNeil BJ. The meaning and use of the area under a receiver operating characteristic (ROC) curve. Radiology. 1982;143(1):29–36.
35. Tibshirani R. The lasso method for variable selection in the cox model. Stat Med. 1997;16(4):385–95.
36. Oyeyemi GM, Ogunjobi EO, Folorunsho AI. On performance of shrinkage methods-a Monte Carlo study. Int J Stat Appl. 2015;5:72–6.
37. Huang YQ, Liang CH, He L, Tian J, Liang CS, Chen X, et al. Development and validation of a radiomics nomogram for preoperative prediction of lymph node metastasis in colorectal cancer. J Clin Oncol. 2016;34(18):2157–64.
38. Wang H, Wang L, Lee EH, Zheng J, Zhang W, Halabi S, et al. Decoding COVID-19 pneumonia: comparison of deep learning and radiomics CT image signatures. Eur J Nucl Med Mol Imaging. 2021;48:1478–86. https://doi.org/10.1007/s00259-020-05075-4.
39. DeLong ER, DeLong DM, Clarke-Pearson DL. Comparing the areas under two or more correlated receiver operating characteristic curves: a nonparametric approach. Biometrics. 1988;44:837–45.

40. Oliveira FPM, Faria DB, Costa DC, Castelo-Branco M, Tavares JMRS. Extraction, selection and comparison of features for an effective automated computer-aided diagnosis of Parkinson's disease based on [123I]FP-CIT SPECT images. Eur J Nucl Med Mol Imaging. 2018;45:1052–62. https://doi.org/10.1007/s00259-017-3918-7.
41. Cuberas-Borrós G, Lorenzo-Bosquet C, Aguadé-Bruix S, Hernández-Vara J, Pifarré-Montaner P, Miquel F, et al. Quantitative evaluation of striatal I-123-FP-CIT uptake in essential tremor and parkinsonism. Clin Nucl Med. 2011;36(11):991–6.
42. Seibyl JP, Marchek KL, Quinlan D, Sheff K, Zoghbi S, Zea-Ponce Y, et al. Decreased single-photon emission computed tomographic {123I}β-CIT striatal uptake correlates with symptom severity in Parkinson's disease. Ann Neurol. 1995;38(4):589–98.
43. Palumbo B, Fravolini ML, Buresta T, Pompili F, Forini N, Nigro P, et al. Diagnostic accuracy of Parkinson disease by support vector machine (SVM) analysis of 123I-FP-CIT brain SPECT data: implications of putaminal findings and age. Medicine. 2014;93(27):e228 (**Baltimore**).
44. Iwabuchi Y, Nakahara T, Kameyama M, Yamada Y, Hashimoto M, Matsusaka Y, et al. Impact of a combination of quantitative indices representing uptake intensity, shape, and asymmetry in DAT SPECT using machine learning: comparison of different volume of interest settings. EJNMMI Res. 2019;9:7. https://doi.org/10.1186/s13550-019-0477-x.
45. Varrone A, Dickson JC, Tossici-Bolt L, Sera T, Asenbaum S, Booij J, et al. European multicentre database of healthy controls for [123I]FP- CIT SPECT (ENC-DAT): age-related effects, gender differences and evaluation of different methods of analysis. Eur J Nucl Med Mol Imaging. 2013;40:213–27.
46. Buchert R, Lange C, Spehl TS, Apostolova I, Frings L, Jonsson C, et al. Diagnostic performance of the specific uptake size index for semi-quantitative analysis of I-123-FP-CIT SPECT: harmonized multi-center research setting versus typical clinical single-camera setting. EJNMMI Res. 2019;9(1):1–13.
47. Nonokuma M, Kuwabara Y, Hida K, Tani T, Takano K, Yoshimitsu K. Optimal ROI setting on the anatomically normalized I-123 FP-CIT images using high-resolution SPECT. Ann Nucl Med. 2016;30:637–44.
48. Lee JY, Lao-Kaim NP, Pasquini J, Deuschl G, Pavese N, Piccini P. Pallidal dopaminergic denervation and rest tremor in early Parkinson's disease: PPMI cohort analysis. Parkinsonism Relat Disord. 2018;51:101–4.
49. Helmich RC, Janssen MJR, Oyen WJG, Bloem BR, Toni I. Pallidal dysfunction drives a cerebellothalamic circuit into Parkinson tremor. Ann Neurol. 2011;69:269–81.
50. Shigekiyo T, Arawaka S. Laterality of specific binding ratios on DAT-SPECT for differential diagnosis of degenerative parkinsonian syndromes. Sci Rep. 2020;10(1):1–8.

Publisher's Note